JOURNAL OF APPLIED CRYSTALLOGRAPHY
ISSN 1600-5767

Hybrid reciprocal lattice: application to layer stress determination in GaAlN/GaN(0001) systems with patterned substrates

Jarosław Z. Domagała,[a] Sérgio L. Morelhão,[b]* Marcin Sarzyński,[c] Marcin Maździarz,[d] Paweł Dłużewski[d] and Michał Leszczyński[c,e]

[a]Institute of Physics, Polish Academy of Sciences, Al. Lotnikow 32/46, 06-668 Warszawa, Poland, [b]Institute of Physics, University of Sao Paulo, CP 66318, CEP 05315-970, São Paulo, SP, Brazil, [c]Institute of High Pressure Physics (UNIPRESS), Polish Academy of Sciences, Sokolowska 29/37, 01-142 Warszawa, Poland, [d]Institute of Fundamental Technological Research (IPPT PAN), Pawińskiego 5 B, 02-106 Warszawa, Poland, and [e]TopGaN Ltd, Sokolowska 29/37, 01-142 Warszawa, Poland. *Correspondence e-mail: morelhao@if.usp.br

Received 1 March 2016
Accepted 15 March 2016

Edited by V. Holý, Charles University, Prague, Czech Republic

Keywords: optoelectronics; Group III–nitride semiconductors; epitaxial growth; X-ray multiple diffraction; interface defects.

Epitaxy of semiconductors is a process of tremendous importance in applied science and in the optoelectronics industry. The control of defects introduced during epitaxial growth is a key point in manufacturing devices of high efficiency and durability. In this work, it is demonstrated how useful hybrid reflections are for the study of epitaxial structures with anisotropic strain gradients due to patterned substrates. High accuracy in detecting and distinguishing elastic and plastic relaxations is one of the greatest advantages of measuring this type of reflection, as well as the fact that the method can be exploited in a symmetric reflection geometry on a commercial high-resolution diffractometer.

1. Introduction

X-ray diffraction is a well established technique for the structural analysis of electronic and optoelectronic devices based on single-crystal substrates and epitaxial layers. However, advances in materials and processing technologies, as well as in X-ray instrumentation (sources, focusing optics and detectors), are creating a demand for new approaches to exploit this excellent tool of structural analysis further. One example of such a material is gallium nitride, which revolutionized the optoelectronics industry in the early 1990s, providing blue photons out of a light-emitting diode (Nakamura *et al.*, 1991). However, it was only very recently that GaN could be synthesized in the form of high-quality single crystals, opening new opportunities in manufacturing electronic and optoelectronic devices (Dwiliński *et al.*, 2008, 2011; Kruszewski *et al.*, 2014; Nakamura, 2015; Muziol *et al.*, 2015). The control of defects in Group III–nitride semiconductor devices is an important issue in terms of processing technologies (Wu & Walukiewicz, 2003; Sarzyński *et al.*, 2006; Czernecki *et al.*, 2007; Gil, 2013), and it must also be addressed when using bulk GaN.

A high-flux X-ray beam impinging on a perfect single crystal, such as the substrate material used in optoelectronic devices, gives rise to intensities measured further away than the ordinary Bragg peaks. Although most of these intensities are caused by diffraction of higher order (Renninger, 1937; Post, 1976), they can also be related to diffuse scattering (Nisbet *et al.*, 2015). Since compact high-flux sources and zero-noise X-ray detectors are becoming affordable as items of equipment in the home laboratory, intentional or accidental observations of such intensity features are expected to become

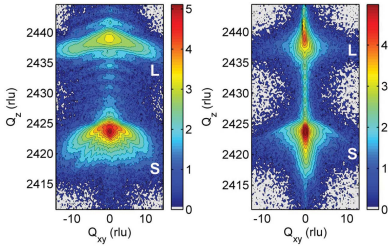

more frequent. Being able to interpret intensity measurements of this kind properly is crucial in the current state of technological development in the research fields of new materials and X-ray metrology.

The occurrence of X-ray rescattering in epitaxial layer/substrate systems, named hybrid reflections, is a phenomenon that has so far only been exploited in cubic (001) crystals (Morelhão & Cardoso, 1993; Morelhão & Domagala, 2007; de Menezes *et al.*, 2009), although it has already been observed in hexagonal systems: the first observation of hybrid reflections in non-cubic materials was reported by Domagała (2010) for a GaN layer on SiC(0001).

Hybrid reflections have their origin in multiple diffraction cases (Isherwood *et al.*, 1981), which can be indexed in bulk materials using available software (Rossmanith, 1999, 2003, 2006). In Group III–nitrides, investigation of multiple diffraction was carried out recently (Kyutt, 2012; Kyutt & Scheglov, 2013). For strain analysis, hybrid reflections offer the benefit of obtaining structural three-dimensional information in diffraction geometries readily suited to most standard high-resolution diffractometers with laboratory (compact) X-ray sources. However, the three-dimensional nature of this phenomenon requires a high level of expertise in single-crystal multiple diffraction geometries in both reciprocal and real space. In this work, we present a general approach to facilitate the exploration of hybrid reflections in non-cubic systems, and we use it to elucidate features in reciprocal space due to strain in AlGaN epitaxial layers grown by metal–organic chemical vapour phase epitaxy (MOVPE) on highly perfect GaN(0001) patterned substrates.

2. Theory

2.1. Bragg cone lines

In real space, the excitation of Bragg reflections is ruled by the relationship $\mathbf{k}\cdot\mathbf{G} = -|\mathbf{G}|^2/2$ between the incident wavevector $\mathbf{k}$ and the diffraction vector $\mathbf{G}$, which gives rise to the Bragg cone (BC) representation of the condition of diffraction illustrated in Fig. 1(*a*). When analysing single crystals with one large face, such as the substrate material employed for epitaxial growth, it is convenient to choose a reference system for describing the direction of the wavevector $\mathbf{k} = -(2\pi/\lambda)[\cos\omega\cos\varphi, \cos\omega\sin\varphi, \sin\omega]$, in terms of the instrumental angles such as the incidence angle ω and azimuth φ; λ is the wavelength of the incident radiation. By projecting the diffraction vector in this reference system, $\mathbf{G} = |\mathbf{G}|[\sin\gamma_G\cos\alpha_G, \sin\gamma_G\sin\alpha_G, \cos\gamma_G]$, with $|\mathbf{G}| = (4\pi/\lambda)\sin\theta_G$, and the BC equation can be replaced by the relationship

$$\cos(\varphi - \alpha_G) = \frac{\sin\theta_G - \sin\omega\cos\gamma_G}{\cos\omega\sin\gamma_G}, \qquad (1)$$

which must be fulfilled by the instrumental angles for Bragg diffraction to take place.

The relationship of equation (1) provides the simplest way of collapsing into a two-dimensional representation the three-dimensional geometry of multiple diffraction in single crystals. It allows an easy understanding of all reflections that can be excited when mapping one particular region of the ω and φ angular space. For instance, Fig. 1(*b*) shows the case of an azimuthal axis with threefold symmetry. Curved lines indicate BCs of asymmetric reflections, while diffraction vectors along the azimuthal axis have their BCs represented as straight lines in the ω–φ graphs (§*A*1) or as the dashed line in Fig. 1(*b*).

In single crystals, the observation of multiple BC lines with a monochromatic and collimated X-ray beam is possible near their intersections, owing to dynamic coupling between the diffracted waves of each reflection (de Menezes *et al.*, 2010; Morelhão & Avanci, 2001). With high-flux sources (synchrotrons, and microfocus beams with focusing optics), even the BC lines of forbidden reflections are visible within a few milliradians of the intersection point. A benchmark demonstration of this long-range dynamic coupling is the intersection of the BC lines from the 002 and 111 reflections in Si(001) crystals (Fig. 2*a*). Rocking curves of the symmetric reflection near this intersection point could present two distinct peaks, instead of the none expected for the forbidden 002 Si reflection, as seen in Fig. 2(*b*). The angle and position of the BC lines predicted by equation (1) are given in Fig. 2(*c*). Monitoring of the intensity distribution over the BC lines, as well as their angle of intersection, has been used to access surface defects and residual strain in nanostructured devices grown on semiconductor substrates (de Menezes *et al.*, 2010; Malachias *et al.*, 2011). For instance, the enhancement of intensity along the 111 BC line above the 002 reflection, $\Delta\omega > 0$ in Fig. 2(*a*), is related to the presence of surface defects that increase the rescattering of the diffracted beam when the 111 reflection is excited, such as reported for GaAs(001) substrates (Freitas *et*

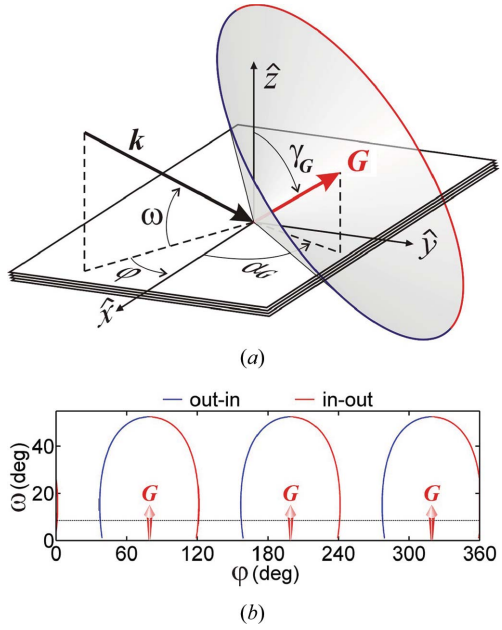

Figure 1
(*a*) The reference system used to describe the incident wavevector **k** and the Bragg cone (BC) of a diffraction vector **G**. (*b*) Excitation conditions in terms of ω and φ angles for equivalent reflections around a threefold symmetry axis. Curved (blue/red) and straight (dashed) lines denote BCs of asymmetric and symmetric reflections, respectively.

al., 2009). Moreover, BC lines have also been seen decorating X-ray images collected by zero-noise detectors, in a process called multiple diffuse scattering (Nisbet *et al.*, 2015).

2.2. Hybrid reflections in hexagonal lattices with strain gradients

In epilayer/substrate systems, the coupling of diffracted waves can be observed further away from the intersection points of the BC lines owing to the rescattering of the diffracted beam by another material with different lattice parameters. The angular conditions for exciting such rescattering events fall over or very near the BC lines of the substrate since, in general, these systems present a small lattice mismatch. A simple ω–φ graph from equation (1) for the substrate is then capable of providing most of the necessary information to locate and use hybrid reflections for stress analysis. After selecting a region of angular space to probe for rescattering events, reciprocal space must be mapped to discriminate the location and shape of hybrid reciprocal-lattice points (RLPs) that might exist there. Their locations in the vicinity of a substrate RLP are given by

$$\Delta\mathbf{P} = h'\Delta\mathbf{a}^* + k'\Delta\mathbf{b}^* + l'\Delta\mathbf{c}^*, \qquad (2)$$

where h', k' and l' are integers, and $\Delta\mathbf{g}^* = \mathbf{g}_L^* - \mathbf{g}_S^*$ (with $\mathbf{g}^* = \mathbf{a}^*$, $\mathbf{b}^*$ or $\mathbf{c}^*$ as the edge vectors of the reciprocal unit cell) characterizes the variation in reciprocal lattice between the two materials, where the subscripts L and S stand for the epilayer and substrate lattices, respectively (Morelhão & Domagala, 2007). In terms of the longitudinal Q_z and transverse Q_{xy} coordinates in reciprocal-space maps, the locations of the hybrid RLPs are

$$Q_z = \Delta\mathbf{P}\cdot\hat{\mathbf{z}} \quad \text{and} \quad Q_{xy} = \Delta\mathbf{P}\cdot\hat{\mathbf{k}}_{xy}, \qquad (3)$$

where $\hat{\mathbf{k}}_{xy}$ is the in-plane direction of the incident wavevector, *i.e.* $\hat{\mathbf{k}}_{xy} = -[\cos\varphi, \sin\varphi, 0]$, according to Fig. 1.

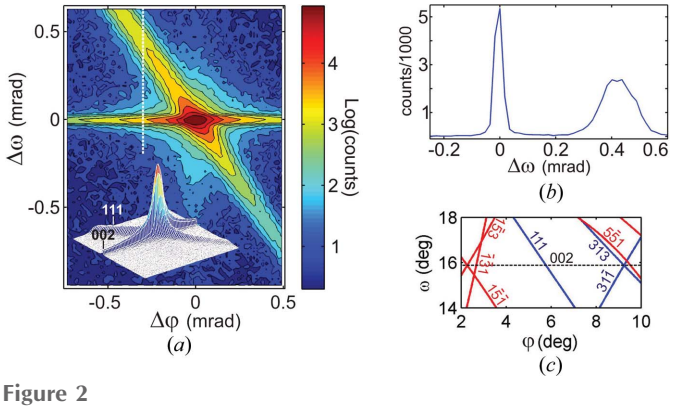

Figure 2
Intersection of Bragg cones in Si(001). (*a*) Two-dimensional intensity profile of the forbidden 002 reflection near the intersection point with the 111 reflection [after Morelhão *et al.* (2002)]. X-rays of 8.34 keV, beam divergences <25 µrad (both axes). (*b*) Rocking curve (ω scan) of the forbidden reflection, showing two peaks at azimuth $\Delta\varphi = -0.3$ mrad, indicated by the dashed white line in part (*a*). (*c*) Nearby BC lines according to equation (1).

Since hybrid RLPs originate in the differences between the two lattices, their shapes are strongly affected by strain gradients, a fact that has been predicted (Morelhão & Domagala, 2007) but not yet observed. On the other hand, in totally relaxed epilayers (in the absence of strain gradients), the shapes of hybrid RLPs are susceptible to the ratio between the in-plane and out-of-plane mosaicities (Morelhão & Domagala, 2007).

Strain gradient and anisotropy can be introduced by grooves in epilayer/substrate materials. Grooves with a flat terrace and oriented along the *y* direction, *e.g.* Fig. 3(*a*), give rise to a nearly constant ε_y strain, while the ε_x strain may vary from a maximum value at the centre of the terraces towards a minimum value at the edges. In hexagonal systems with a (001) surface and grooves along the $[\bar{1}10]$ direction, strain anisotropy is also implied in unit cells with a distorted basal plane where the γ angle differs from 120° by $\Delta\gamma$ (Fig. 3*b*). In terms of the in-plane strain components, strained epilayer unit cells are described by

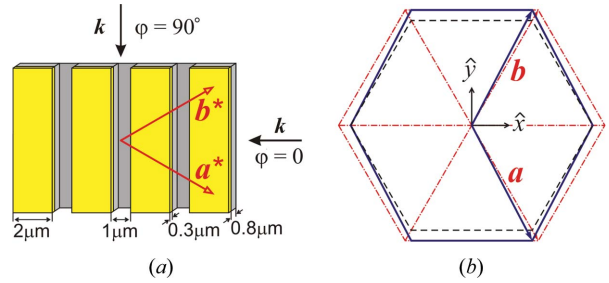

Figure 3
(*a*) An AlGaN/GaN(001) sample with grooves along the $[\bar{1}10]$ crystallographic direction. (*b*) The basal plane of the epilayer unit cell when fully strained (dash-dotted line), relaxed (dashed line) or partially relaxed (solid line) along the *x* direction only.

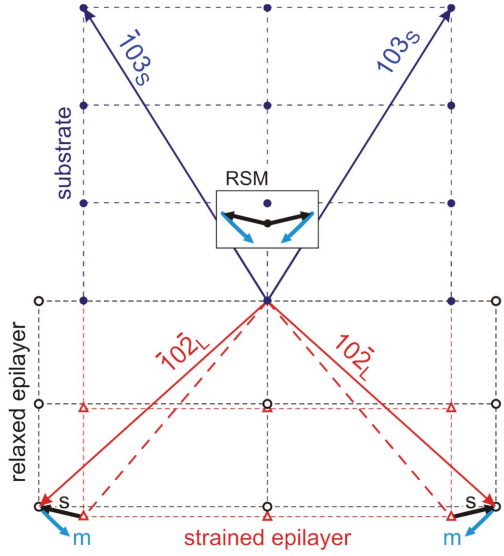

Figure 4
Scheme of how the strain gradient (arrows s) and misorientation (arrows m) of the epilayer diffraction vectors are seen when mapping hybrid reflections in reciprocal space. Filled circles, open circles and triangles stand for substrate, relaxed epilayer and fully strained epilayer RLPs, respectively.

$$\begin{aligned}\frac{\Delta a}{a} &= \frac{\Delta b}{b} = \frac{\varepsilon_x + \varepsilon_y}{2} + \cos\gamma\frac{\varepsilon_x - \varepsilon_y}{2},\\ \frac{\Delta c}{c} &= \frac{C_{13}}{C_{33}}(\varepsilon_x + \varepsilon_y),\\ \Delta\gamma &= -\sin\gamma(\varepsilon_x - \varepsilon_y).\end{aligned} \tag{4}$$

Elastic strain relaxation at groove terraces – without misfit dislocations – can be accompanied by a deflection of the lattices, causing misorientation of the diffraction vectors near the groove edges. A pictorial scheme accounting for both effects, a strain gradient and a misorientation of relaxed epilayer regions, is shown in Fig. 4. By mapping reciprocal space around the 001 substrate RLP with the sample at an appropriate azimuth, hybrids such as $103_S + \bar{1}0\bar{2}_L$ and $10\bar{2}_L + \bar{1}03_S$ will have shapes revealing the presence of these two effects.

For easy access to the in-plane strain values from a measure of Q_{xy} in either reciprocal space maps (RSMs) or transverse scans, equation (3) is rewritten as a function of the in-plane lattice mismatches along the x and y directions, *i.e.* $\varepsilon_x^S = (\Delta d/d)_{[110]}$ and $\varepsilon_y^S = (\Delta d/d)_{[\bar{1}10]}$, respectively. This results in

$$Q_{xy} = \frac{2\pi}{a_S}(h' + k')\cos\varphi\varepsilon_x^S + \frac{2\pi}{a_S 3^{1/2}}(-h' + k')\sin\varphi\varepsilon_y^S, \tag{5}$$

which can then be assigned to the epilayer strain components by means of $a_S(1 + \varepsilon_{x,y}^S) = a_{0,L}(1 + \varepsilon_{x,y})$, where a_S and $a_{0,L}$ are the unstrained substrate and epilayer in-plane lattice parameters, respectively.

3. Experimental

3.1. Sample preparation

AlGaN epilayers were deposited by MOVPE on hexagonal GaN(001) substrates (Dwiliński *et al.*, 2011). The nominal epilayer thickness was 0.3 µm. Lithography was carried out after growth to produce square grooves, as indicated in Fig. 3(*a*). Here, Bragg planes and reflections are indicated by three indexes regarding the primitive unit cell (*e.g.* Fig. 3*b*).

3.2. X-ray measurements

X-ray data were collected on a Philips X'Pert-MRD high-resolution diffractometer with a Cu tube and proportional gas detector. Incident beam optics: X-ray mirror; four-crystal asymmetric 220 Ge monochromator ($\Delta\lambda/\lambda = 5 \times 10^{-5}$); beam divergences 0.005 and 2° in the incidence plane and axial direction, respectively; beam size at sample position 0.28 × 1 mm. Diffracted beam optics: three-bounce 220 Ge analyser crystal for triple-axis or 1/4° slit for double-axis diffractometry. Extra features: diffraction vectors of symmetric reflections were precisely aligned with the φ rotation axis by a mechanical device assembled on the standard sample holder of the diffractometer.

4. Results and discussion

4.1. Longitudinal scans

One-dimensional reciprocal space scans along the c axis, *i.e.* $2\theta/\omega$ scans, were carried out as a function of the sample azimuth and they reveal hybrid RLPs with index $l' = -2, -1, 0$ and 1 (Fig. 5*a*). The $h'k'l'$ indexes of the hybrids are inferred from the nearby BC lines, shown in Fig. 5(*b*). The BC lines of indexes hkl where $l \leq 0$ give rise to hybrids of indexes $h'k'l' = hkl$, while $h' = -h$, $k' = -k$ and $l' = 1 - l$ are the hybrid indexes for the BC lines where $l \geq 1$. For instance, $10\bar{2}$ and $\bar{1}0\bar{2}$ are hybrid indexes at $\varphi = 10°$ in Fig. 5(*a*), and they are excited by the $10\bar{2}$ and 103 BC lines, respectively. In other words, hybrids have the same indexes as the epilayer reflections taking part in the rescattering events, such as in the illustration in Fig. 4. Indexes with $l' = 0$ are hybrids coincidental with n-beam diffraction of the substrate, and $l' = 1$ are the epilayer multiple-beam diffractions. Therefore, the actual hybrids revealed by the $2\theta/\omega$ scans in Fig. 5(*a*) are those of $l' = -2$ and -1. Their positions along the c axis are explained by a perpendicular lattice mismatch $\varepsilon_z^S = (c_L - c_S)/c_S \simeq -7.1 \times 10^{-3}$, which follows from

$$\begin{aligned}2\Delta c^* &= 2\left(\frac{2\pi}{c_L} - \frac{2\pi}{c_S}\right)\\ &\simeq (4\pi/\lambda)[\sin(17.097/2) - \sin(16.850/2)]\\ &= 0.0174\ \text{Å}^{-1}.\end{aligned} \tag{6}$$

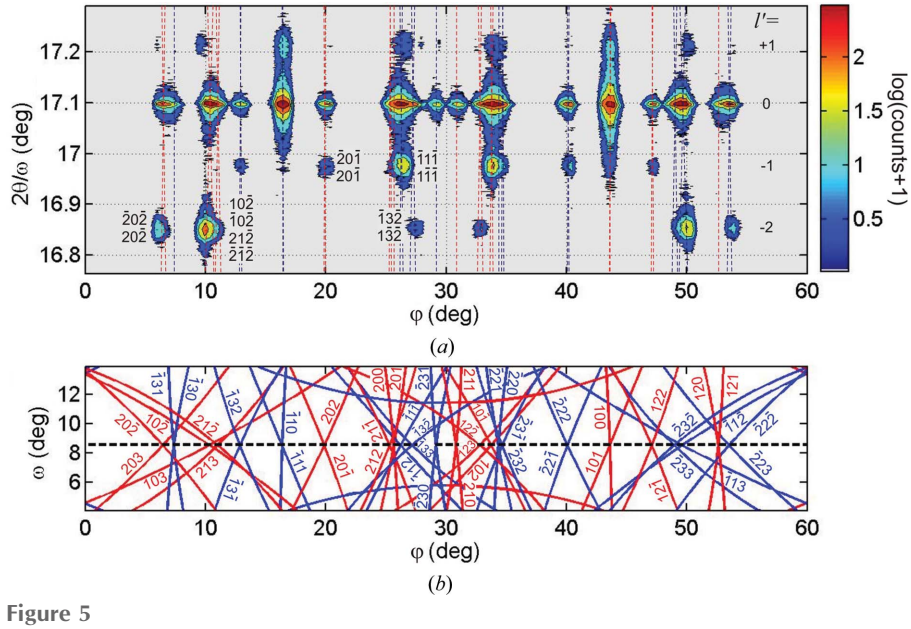

Figure 5
(*a*) $2\theta/\omega$ scan of the forbidden 001 GaN reflection as a function of the sample azimuth. Reference direction [110] ($\varphi = 0$). The $h'k'l'$ indexes are explained in the text. (*b*) BC lines in GaN(001), also shown in part (*a*) as dashed lines after appropriate rescaling.

According to equations (2) and (3), hybrids with nonzero h' and k' indexes can be seen on one-dimensional scans along the c axis in two situations: (i) when there are fully strained epilayer regions in which $\Delta a^* = \Delta b^* = 0$; or (ii) when the projection of $\Delta\mathbf{P}$ along $\hat{\mathbf{k}}_{xy}$ is null. Since the hybrids in Fig. 5(*a*) are seen at different azimuths from $\varphi = 10$ to 50°, the in-plane lattice mismatches are null or very small, as can be checked by applying equation (5) to the observed hybrids. A direct determination of the epilayer composition is therefore possible in such a case. By using tabulated values for the GaN and AlN compounds (§*A*2), we can state that, in a fully strained $Al_xGa_{1-x}N$ epilayer on GaN(001), $x \simeq -19.4\varepsilon_z^S$, and the above value of the lattice mismatch leads to $x = 0.138 \pm 0.004$.

4.2. Reciprocal space mapping

An RSM measured at $\varphi = 10^\circ$ is presented in Fig. 6(*a*). The strongest hybrid intensity occurs at $Q_{xy} = 0$, evidencing that most of the epilayer regions fully strained (no in-plane lattice mismatch) with respect to the substrate lattice are taking part in the rescattering events. However, the pattern formed by the weak intensity distribution around the hybrid spot closely resembles the expected pattern schematized in Fig. 4 for the case of a gradual release of strain and misorientation of relaxed epilayer regions. A similar pattern is also seen in Fig. 6(*b*), where an RSM measured at $\varphi = 34^\circ$ encompasses hybrids with index $l' = -1$. The RSMs in Figs. 6(*c*) and 6(*d*) measure equivalent reflections, but at azimuths increased by 60° and hence closer to the y direction. The patterns of weak intensity in these latter maps are observed to shrink according to $\cos\varphi$ with respect to those in Figs. 6(*a*) and 6(*b*). This agrees with a preferential relaxation of the epilayer along the [110] direction perpendicular to the grooves.

From one RSM to another, a modification of the two-dimensional intensity profiles of the substrate 001 n-beam diffraction spots can also be observed. The streaks of weak intensity from the substrate are nearly parallel to those around the hybrid spots, and all such streaks are indicated by arrows in Figs. 6(*a*) and 6(*b*). This confirms that both lattices have deviated from flatness in the groove terraces, indicating that the relaxation caused by the grooves has an elastic character.

Along the grooves, some misfit dislocations (plastic relaxation) may have been introduced in the epilayer, judging

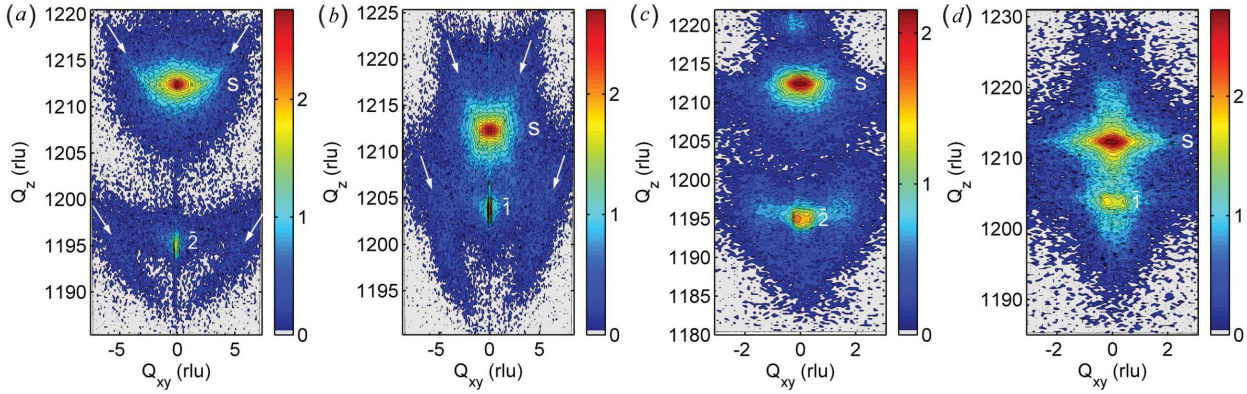

Figure 6
Reciprocal space maps of the forbidden 001 reflection in AlGaN/GaN(001) at different azimuths: (*a*) $\varphi = 10^\circ$, (*b*) $\varphi = 34^\circ$, (*c*) $\varphi = 70^\circ$ and (*d*) $\varphi = 94^\circ$. Substrate n-beam diffraction spots are labelled S, while hybrid spots are labelled by their l' index, $\bar{1}$ or $\bar{2}$. Streaks of weak intensity mentioned in the text are indicated by arrows. Colour bars are log(counts+1). Reciprocal lattice units (rlu) = 0.001 Å^{-1}.

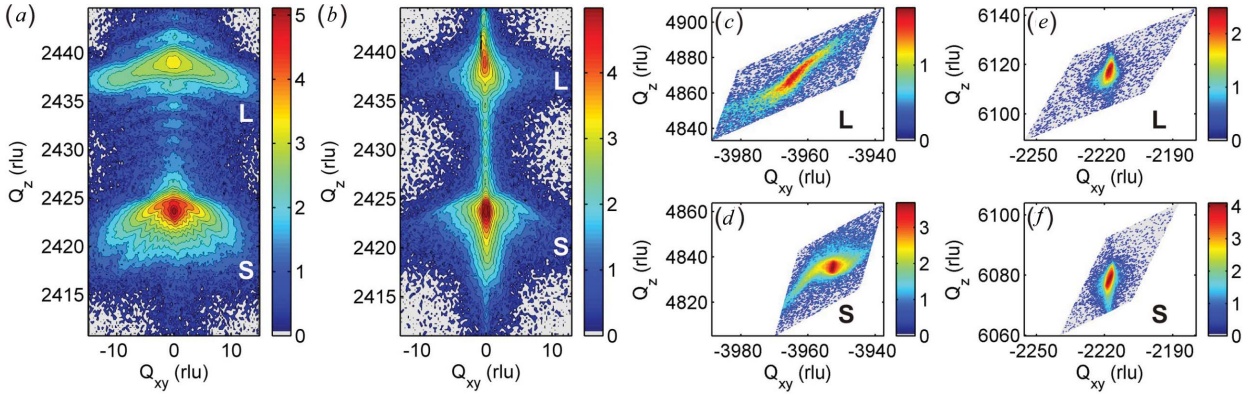

Figure 7
Reciprocal space maps of different reflections in AlGaN/GaN(001): (*a*) 002 at $\varphi = 0$, (*b*) 002 at $\varphi = 90^\circ$, (*c*) and (*d*) $\bar{1}\bar{1}4$, $\varphi = 0^\circ$, (*e*) and (*f*) $1\bar{1}5$, $\varphi = 90^\circ$. The labels L and S denote epilayer and substrate reflections, respectively. Colour bars are log(counts+1). Reciprocal lattice units (rlu) = 0.001 Å^{-1}.

by the small split in the hybrid spots that can be seen in Figs. 6(*c*) and 6(*d*). For a split of $(0.57 \pm 0.01) \times 10^{-3}$ Å^{-1} between the hybrids $01\bar{1}$ and $0\bar{1}\bar{1}$ at $\varphi = 94°$ (Fig. 6*d*), equation (5) provides a lattice mismatch $\varepsilon_y^S = -(2.4 \pm 0.2) \times 10^{-4}$ along the grooves. This corresponds to an epilayer relaxation of about $7.3 \pm 0.6\%$ when taking $a_S = 3.1885$ Å and $a_{0,L} = 3.178$ Å (composition $x = 0.138$).

For the sake of comparison, the usual procedure for strain analysis in epilayer/substrate systems has also been carried out. RSMs of symmetric and asymmetric reflections at azimuths perpendicular ($\varphi = 0$) and parallel ($\varphi = 90°$) to the grooves are shown in Fig. 7. The correlation between deflection and strain of the two lattices, mostly along the *x* direction, is clearly seen in Figs. 7(*a*) and 7(*b*). This is the behaviour expected from finite element analysis (§*A*3). Asymmetric $\bar{1}14$ reflections in Figs. 7(*c*) and 7(*d*) evidence epilayer relaxation perpendicular to the grooves, while the asymmetric $1\bar{1}5$ reflections in Figs. 7(*e*) and 7(*f*) show a fully strained epilayer along the grooves. An in-plane relaxation of 50% is implied by a perpendicular lattice mismatch of $\varepsilon_z^S = -6.2 \times 10^{-3}$ (composition $x = 0.138$, see §*A*2), and this is the experimental value obtained by direct measurement of the spot-to-spot distance along Q_z in Fig. 7(*a*), *i.e.*

$$\varepsilon_z^S = -(2439.1 - 2423.7)/2423.7 = -(6.4 \pm 0.2) \times 10^{-3}. \quad (7)$$

In-plane lattice mismatches accessed *via* asymmetric reflections (Figs. 7*c*–7*f*) have an accuracy limit not less than 5×10^{-4}. This is imposed by the fact that the diffraction spots are relatively broad regarding their separation in reciprocal space. Thus, from the asymmetric reflections in $Al_{0.14}Ga_{0.86}N$/GaN(001) it is not possible to detect an epilayer relaxation of less than 15%. In contrast, hybrid reflections show an accuracy of 2×10^{-5} in detecting in-plane lattice mismatch, and hence have the capability of probing variations of 1% in the epilayer relaxation. Such accuracy is corroborated by the fact that hybrid reflections are rescattering processes through the epilayer/substrate interface. Elastic relaxation of lattice mismatch through the interface takes place on a much smoother length scale than an abrupt plastic deformation caused by misfit dislocations. Therefore, the sharp splits in Q_{xy} of the hybrid spots seen in Figs. 6(*c*) and 6(*d*) are strong evidence of plastic relaxation, although to a degree that is hard to detect by standard measurements of asymmetric reflections even when a detailed dynamic X-ray diffraction simulation is carried out (Minkevich *et al.*, 2011).

5. Conclusion

A patterned GaN(001) hexagonal substrate was very successful in promoting the elastic relaxation of a 0.3 µm thick $Al_{0.14}Ga_{0.86}N$ epilayer in the direction perpendicular to the lithographed stripes, preventing misfit dislocations with a Burgers vector perpendicular to the stripes in the structure. However, along the stripes, a relaxation of about 7% could be credited to the presence of misfit dislocations. The X-ray diffraction method demonstrated and used in this work exploits second-order scattering events at the epilayer/substrate interface, which allows detection of in-plane lattice mismatches with an accuracy that is at least ten times better than that obtained by measuring single asymmetric reflections of the layer and substrate lattices separately. Direct determination of the epilayer composition by simple $2\theta/\omega$ scans in a symmetric reflection geometry is also possible. Moreover, the proposed general approach to locate and index such rescattering events greatly facilitated the application of the method to hexagonal crystal structures.

APPENDIX *A*

A1. Two-dimensional Bragg cone representation

To project the crystal reciprocal space onto the reference system used to describe the instrumental ω and φ angles, $\mathbf{A} = H\mathbf{a}^* + K\mathbf{b}^* + L\mathbf{c}^*$ is taken as the reciprocal vector aligned along the φ rotation axis, and $\mathbf{B} = B_1\mathbf{a}^* + B_2\mathbf{b}^* + B_3\mathbf{c}^*$ is the direction in reciprocal space that lies in the incident plane (pointing upstream) when $\varphi = 0$; then $\hat{\mathbf{x}} = \hat{\mathbf{y}} \times \hat{\mathbf{z}}$, $\hat{\mathbf{y}} = \hat{\mathbf{z}} \times \mathbf{B}/|\mathbf{B}|$ and $\hat{\mathbf{z}} = \mathbf{A}/|\mathbf{A}|$. From a full list of reflection indexes with no null structure factors (Morelhão, 2015), the diffraction vectors $\mathbf{G}$ are taken and their polar and azimuthal angles calculated as $\gamma_G = \cos^{-1}(\hat{\mathbf{z}} \cdot G/|\mathbf{G}|)$ and $\alpha_G = \tan^{-1}(\hat{\mathbf{y}} \cdot G/\hat{\mathbf{x}} \cdot G)$, respectively; α_G must be accounted for in the four quadrants. Equation (1) provides two solutions for the azimuth φ as a function of the incidence angle ω, which are plotted as the out–in and in–out BC lines in the ω–φ graphs, *e.g.* Figs. 1(*b*), 2(*c*) and 5(*b*).

A2. Strain calculation in the $Al_xGa_{1-x}N$ alloy

By applying Vegard's law to the AlN and GaN lattice and elastic constants in Table 1, the perpendicular lattice mismatch of an $Al_xGa_{1-x}N$ epilayer on GaN(001) as a function of composition x and average in-plane relaxation $\langle R \rangle$ has a linear behaviour that, for $x < 0.2$ (Fig. 8), can be summarized as

$$\varepsilon_z^S = (\Delta c/c) = -(5.16 - 1.24\langle R \rangle) \times 10^{-2}\, x. \quad (8)$$

For instance, an epilayer with composition $x = 0.138$ would have $\varepsilon_z^S = -7.1 \times 10^{-3}$ when fully strained with $\langle R \rangle = 0$, and

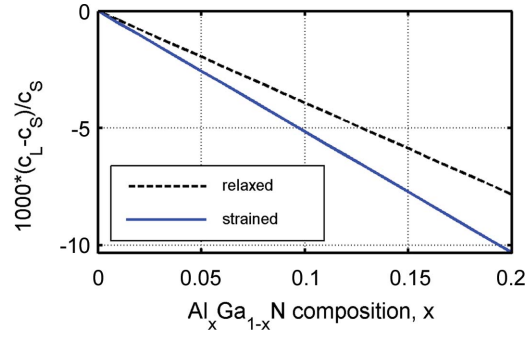

Figure 8
The perpendicular lattice mismatch in relaxed and fully strained $Al_xGa_{1-x}N$ on GaN(001) as a function of composition x.

Table 1
Lattice and elastic constants of AlN and GaN compounds (Leszczyński *et al.*, 1999; Paszkowicz *et al.*, 2004; Schwarz *et al.*, 1997; Wright, 1997).

	a (Å)	c (Å)	C_{13}	C_{33}
GaN	3.1885	5.1850	103	405
AlN	3.112	4.982	108	373

$\varepsilon_z^S = -6.2 \times 10^{-3}$ when totally relaxed along one in-plane direction, *i.e.* $\langle R \rangle = 0.5$.

A3. Elastic mismatch accommodation at the AlGaN/GaN interface by finite element calculation

A nonlinear finite element problem was solved with the use of a chemo-hyperelastic user element coded into the *FEAP* program (Dłużewski *et al.*, 2004; Jurczak & Dłużewski, 2016; Maździarz, 2010). The anisotropic hookian model used is based on the Hencky measure of lattice strain; the chemo-elastic coupling is modelled with the use of Vegard's law. In this approach, a three-dimensional displacement field is spanned on 27 nodes (brick elements) by means of second-order Lagrangean shape functions. Only eight corner nodes are used for modelling the aluminium fraction field stored in nodes on the fourth degree of freedom and spanned by means of first-order Lagrangian shape functions. Such a continuous distribution of elastic and chemical fields was essential, mainly for modelling the residual stresses in the interfacial zone. The AlGaN/GaN zone was discretized by means of a very narrow single layer of finite elements of thickness 10 nm (see Fig. 9). The first three deformation freedoms in the nodes correspond to the displacements x, y and z, while the fourth degree was used to input the aluminium molar fraction. A plane strain boundary condition in the y direction was imposed for all nodes of the mesh. Because of symmetry, the displacements in the x direction were fixed on external surfaces in the x direction. At the bottom, the mesh was fixed in the z direction.

Acknowledgements

The authors acknowledge support in part by the project WISEGaN sponsored by the Polish National Centre for Research and Development (NCBiR) in the framework of the Japan-V4 programme (No. N519 647640) funded by the Polish Ministry of Science and Higher Education. SLM also acknowledges the Brazilian funding agency CNPq (grant Nos. 306982/2012-9 and 452031/20150).

References

Czernecki, R., Krukowski, S., Targowski, G., Prystawko, P., Sarzynski, M., Krysko, M., Kamler, G., Grzegory, I., Leszczyński, M. & Porowski, S. (2007). *Appl. Phys. Lett.* **91**, 231914.

Dłużewski, P., Maciejewski, G., Jurczak, G., Kret, S. & Laval, J.-Y. (2004). *Comput. Mater. Sci.* **29**, 379–395.

Domagała, J. Z. (2010). *10th Biennial Conference on High-Resolution X-Ray Diffraction and Imaging (XTOP2010)*, Warwick, UK, 20–23 September 2010, Book of Abstracts, p. 39. University of Warwick.

Dwiliński, R., Doradziński, R., Garczyński, J., Sierzputowski, L., Kucharski, R., Zaja, M., Rudziński, M., Kudrawiec, R., Strupiński, W. & Misiewicz, J. (2011). *Phys. Status Solidi A*, **208**, 1489–1493.

Dwiliński, R., Doradziński, R., Garczyński, J., Sierzputowski, L., Puchalski, A., Kanbara, Y., Yagi, K., Minakuchi, H. & Hayashi, H. (2008). *J. Cryst. Growth*, **310**, 3911–3916.

Freitas, R. O., Quivy, A. A. & Morelhão, S. L. (2009). *J. Appl. Phys.* **105**, 036104.

Gil, B. (2013). *III–Nitride Semiconductors and their Modern Devices.* Oxford University Press.

Isherwood, B. J., Brown, B. R. & Halliwell, M. A. G. (1981). *J. Cryst. Growth*, **54**, 449–460.

Jurczak, G. & Dłużewski, P. (2016). *Comput. Mater. Sci.* **111**, 197–202.

Kruszewski, P., Prystawko, P., Kasalynas, I., Nowakowska-Siwinska, A., Krysko, M., Plesiewicz, J., Smalc-Koziorowska, J., Dwiliński, R., Zajac, M., Kucharski, R. & Leszczyński, M. (2014). *Semicond. Sci. Tech.* **29**, 075004.

Kyutt, R. N. (2012). *Pis'ma Zh. Tekh. Fiz.* **38**, 77–85.

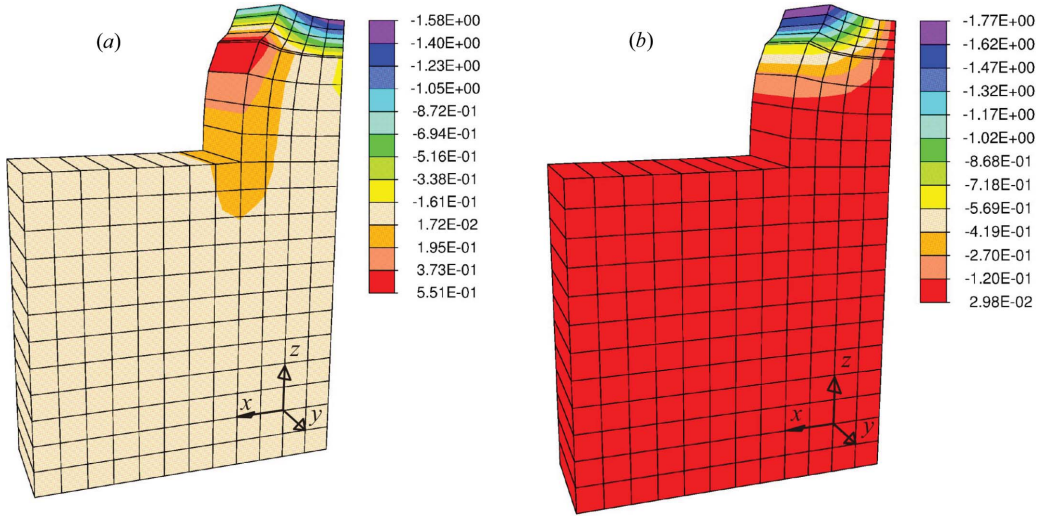

Figure 9
Finite element analysis, showing the deformation with respect to the GaN bulk crystal, (*a*) along z and (*b*) along x. Mesh view with 100 times enlarged displacements to visualize better the character of the lattice distortion.

Kyutt, R. & Scheglov, M. (2013). *J. Appl. Cryst.* **46**, 861–867.
Leszczyński, M., Prystawko, P., Suski, T., Lucznik, B., Domagała, J., Bak-Misiuk, J., Stonert, A., Turos, A., Langer, R. & Barski, A. (1999). *J. Alloy Compd.* **286**, 271–275.
Malachias, A., Freitas, R., Morelhão, S. L., Magalhães-Paniago, R., Kycia, S. & Medeiros-Ribeiro, G. (2011). *Handbook of Instrumentation and Techniques for Semiconductor Nanostructure Characterization*, edited by R. Haight, F. M. Ross & J. B. Hannon, Vol. 1, pp. 211–279. Washington, DC: World Scientific.
Maździarz, M. (2010). *Comput. Model. Eng. Sci.* **66**, 1–24.
Menezes, A. S. de, dos Santos, A. O., Almeida, J. M. A., Bortoleto, J. R. R., Cotta, M. A., Morelhão, S. L. & Cardoso, L. P. (2009). *Phys. Status Solidi B*, **246**, 544–547.
Menezes, A. S. de, dos Santos, A. O., Almeida, J. M. A., Bortoleto, J. R. R., Cotta, M. A., Morelhão, S. L. & Cardoso, L. P. (2010). *Cryst. Growth Des.* **10**, 3436–3441.
Minkevich, A. A., Fohtung, E., Slobodskyy, T., Riotte, M., Grigoriev, D., Schmidbauer, M., Irvine, A. C., Novák, V., Holý, V. & Baumbach, T. (2011). *Phys. Rev. B*, **84**, 054113.
Morelhão, S. L. (2015). *Computer Simulation Tools for X-ray Analysis.* Heidelberg: Springer.
Morelhão, S. L. & Avanci, L. H. (2001). *Acta Cryst.* A**57**, 192–196.
Morelhão, S. L., Avanci, L. H., Quivy, A. A. & Abramof, E. (2002). *J. Appl. Cryst.* **35**, 69–74.
Morelhão, S. L. & Cardoso, L. P. (1993). *J. Appl. Phys.* **73**, 4218–4226.
Morelhão, S. L. & Domagala, J. Z. (2007). *J. Appl. Cryst.* **40**, 546–551.
Muziol, G., Siekacz, M., Turski, H., Wolny, P., Grzanka, S., Grzanka, E., Feduniewiczmuda, A., Borysiuk, J., Sobczak, K., Domagała, J., Nowakowska-Siwińska, A., Makarowa, I., Perlin, P. & Skierbiszewski, C. (2015). *J. Cryst. Growth*, **425**, 398–400.
Nakamura, S. (2015). *Engineering*, **1**, 161.
Nakamura, S., Mukai, T. & Senoh, M. (1991). *Jpn. J. Appl. Phys.* **30**, L1998–L2001.
Nisbet, A. G. A., Beutier, G., Fabrizi, F., Moser, B. & Collins, S. P. (2015). *Acta Cryst.* A**71**, 20–25.
Paszkowicz, S., Podsiadło, W. & Minikayev, R. (2004). *J. Alloy Compd.* **382**, 100–106.
Post, B. (1976). *Acta Cryst.* A**32**, 292–296.
Renninger, M. (1937). *Z. Phys.* **106**, 141–176.
Rossmanith, E. (1999). *J. Appl. Cryst.* **32**, 355–361.
Rossmanith, E. (2003). *J. Appl. Cryst.* **36**, 1467–1474.
Rossmanith, E. (2006). *Acta Cryst.* A**62**, 174–177.
Sarzyński, M., Kryśko, M., Targowski, G., Czernecki, R., Sarzyńska, A., Libura, A., Krupczyński, W., Perlin, P. & Leszczyński, M. (2006). *Appl. Phys. Lett.* **88**, 121124.
Schwarz, R. B., Khachaturyan, K. & Weber, E. R. (1997). *Appl. Phys. Lett.* **70**, 1122.
Wright, A. F. (1997). *J. Appl. Phys.* **82**, 2833.
Wu, J. & Walukiewicz, W. (2003). *Superlattices Microstruct.* **34**, 63–75.